PAPER

Mapping in-plane orientational order and correlation lengths in molecular films using azimuthal-scanning vibrational sum-frequency generation microscopy

Nasim Mirzajani,† Ben John, [ID] † Martin Wolf, [ID] Martin Thämer [ID] and Alexander P. Fellows [ID] *

Self-assembled molecular films are omnipresent in nature, where their highly ordered anisotropic packing structures play a crucial role in governing the macroscopic properties and functional behavior of interfaces. Beyond their local anisotropy, these molecular structures can also often display pronounced heterogeneity and long-range in-plane packing order – from the molecular-to-microscopic scale. Accessing this complex structural information experimentally, however, is a veritable challenge. Phase-resolved sum-frequency generation (SFG) microscopy has recently emerged as a powerful technique for elucidating these structural aspects of thin films, but many properties have so far remained inaccessible such as details about the width and shape of the microscopic orientational distribution. In this work, we show how implementing an azimuthal-scanning approach in SFG microscopy can be used to overcome this limitation by yielding the full in-plane orientational distribution, going far beyond extracting the average molecular orientation. Specifically, by analyzing the complete set of rotational frequencies that arise from the azimuthal dependency, we show through simulated data how they are differently affected by any in-plane orientational disorder or deviation from perfect crystallinity, as well as more complex packing such as bimodal arrangements. This hence offers a route to elucidate the details of the orientational distribution. We then apply this concept to a model membrane comprised of a phase-separated mixed phospholipid monolayer, demonstrating that the molecules within the condensed domains possess micron-scale orientational correlations but nevertheless display substantial diversity in their in-plane orientation, showing both a non-negligible spread in the molecular orientational distribution, as well as profoundly different orientations for their two tail-groups. Overall, this showcased example highlights the potential for this method in future investigations on the role packing structure plays in the functional behavior in lipid membranes. Beyond this, the theoretical concepts

Fritz-Haber-Institut der Max-Planck-Gesellschaft, Faradayweg 4-6, Berlin, 14195, Germany. E-mail: fellows@fhi-berlin.mpg.de; Tel: +49 30 8413 5140

† These authors contributed equally to this work.

Faraday Discussions

presented in this work can be extended to a wide range of systems, from molecular samples to phononic materials, and thus has potential to open-up new directions in the structural elucidation at interfaces.

1 Introduction

Anisotropy in thin films plays a pivotal role in determining their functional behavior at interfaces, influencing phenomena such as charge distribution and transport in photovoltaic systems and the modulation of the surface energy and work function in self-assembled monolayers.[1–3] Likewise, biological membranes harness anisotropy within their lipid bilayers to facilitate the orientation-dependent insertion and activity of transmembrane proteins, including ion channels and receptors.[4,5] This coupling between molecular organization and function also extends laterally across the membrane, where compositional anisotropy gives rise to distinct ordered and disordered regions, known as lipid rafts, that serve as dynamic platforms for regulating cell signalling processes and trafficking membrane components.[6,7] Although the significance of this in-plane anisotropy is well-established, the precise molecular orientations and conformations that determine the packing arrangements remain poorly understood.

To study such complex systems, it is essential to obtain several complementary pieces of information about the constituents of the molecular films, including their identity, conformation, molecular orientation, long-range packing structure, and the degree of order in their assembly. We have recently demonstrated the possibility of experimentally extracting many aspects of the 3D structure of molecules in monolayer lipid films using phase-resolved sum-frequency generation (SFG) microscopy.[8–10] Molecular recognition is achieved by probing the vibrational resonances of specific functional groups within the lipid molecules through their characteristic spectral fingerprints. Furthermore, analysis of the signal variation under different polarizations can give information on the molecular orientation.[11,12] Beyond these capabilities that are common to all vibrational spectroscopies, SFG is uniquely suited to the structural investigation of these complex systems due to its nonlinear origin and highly restrictive symmetry selection rules.

As a second-order nonlinear optical technique, SFG signals are governed by the symmetry conditions of the second-order susceptibility tensor, which importantly changes sign upon orientational inversion.[13–15] Therefore, phase-resolved SFG can not only assess the orientation of molecules through polarization selection, but even reveal their absolute directionality (*e.g.* up *vs.* down) through the sign of the output field.[13,16–18] Furthermore, while an individual molecule need only lack centrosymmetry to generate an SFG signal, an ensemble of such molecules must also be sufficiently ordered so that their individual responses do not cancel due to isotropy. Thus, SFG is sensitive not only to molecular asymmetry but also to the degree of order in the packing structure. For this reason, vibrational SFG has been established as a powerful method for probing different aspects of the anisotropic structure in molecular films and at interfaces.[19–29] Therefore, by combining these unique capabilities of SFG with spatial resolution in an optical microscope, phase-resolved SFG microscopy is the ideal tool for studying the many different

aspects of the heterogeneous molecular structure in complex molecular films.[8,19,22,30–34]

In our previous work, we also showed that combining phase-resolved SFG microscopy with azimuthal (rotational) scanning of the sample is a powerful method for characterizing the 3D packing structure.[8,9] Specifically, it can yield both the in-plane (x, y; see Fig. 1(a)) orientation of specific bonds (modes) from the rotational phase of the first nonzero rotational frequency (1st-fold) as well as their out-of-plane tilt angle with respect to the surface normal (z-axis in Fig. 1(a)). As a case study in extracting this information, we examined a model membrane system composed of a mixture of 1,2-dipalmitoyl-sn-glycero-3-phosphocholine (DPPC) and d_{82}-1-palmitoyl-2-oleoyl-glycero-3-phosphocholine (d-POPC) molecules using the SFG microscope.[8,9] In such a mixture, the lipids spontaneously form densely-packed, ordered regions of liquid condensed (LC) phase that appear
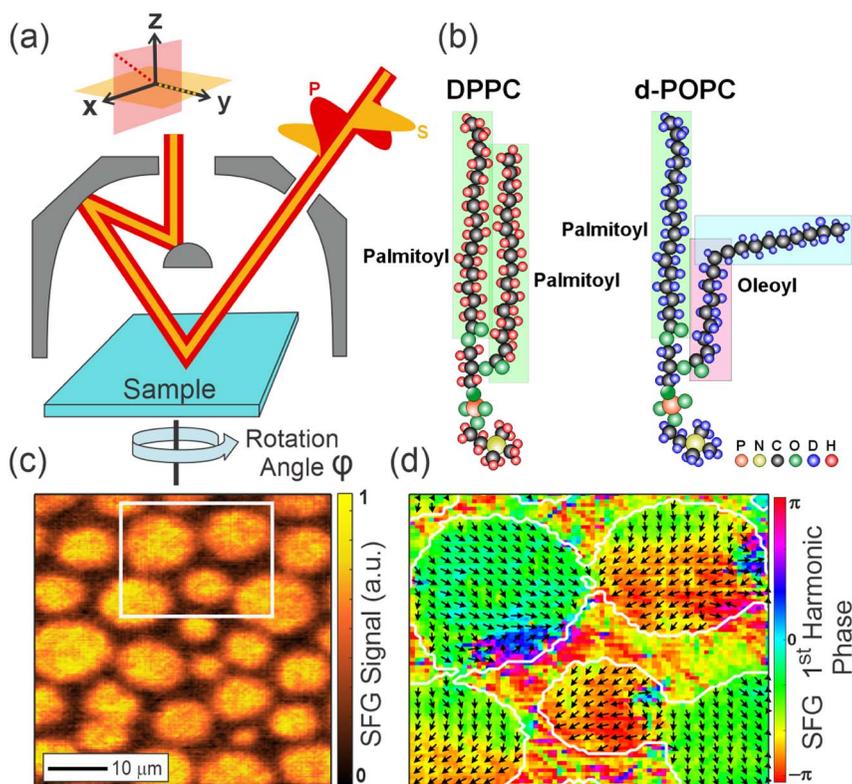

Fig. 1 (a) Schematic of the SFG microscope, depicting the measurement polarization geometry (SSP) in the lab frame, and the azimuthal rotation of the sample by angle φ. (b) Molecular structure of DPPC and deuterated POPC (d-POPC). (c) SFG microscope image showing the roughly circular liquid condensed (LC) domains enriched in DPPC surrounded by the liquid expanded (LE) phase enriched in d-POPC. The contrast stems from the CH_3 symmetric stretch mode and thus is a measure of the out-of-plane order and density of DPPC (since d-POPC yields no signals in this frequency range). (d) Map of average in-plane molecular orientation Φ in the DPPC domains marked by the white rectangle in (c), as determined by the phase of the first rotational frequency.

as circular domains enriched in DPPC within an unordered liquid expanded (LE) phase enriched in d-POPC. Fig. 1 shows the structure of both molecules as well as the heterogeneous LC-LE phase structure imaged with the SFG microscope in the SSP polarization combination. In-depth analysis of the in-plane structure within the LC domains previously showed the DPPC to exhibit a chiral packing structure on the mesoscopic scale.[8] This ordered in-plane packing arrangement is once again highlighted in Fig. 1(d) which shows the 1st-fold rotational phase along with arrows corresponding to the average molecular direction. This in-plane packing structure clearly necessitates a highly ordered arrangement with strong correlations between the orientations of neighboring molecules on shorter scales that translate to such substantial long-range order.

In this work, we delve deeper into the analysis of the in-plane molecular packing structure, going far beyond the analysis of the average in-plane orientation that is accessible from the phase of the 1st-fold rotational frequency, which was the focus of previous work.[8] Specifically, we aim towards gaining insight into the full in-plane orientational distribution. Using theoretical simulations, we first discuss how information about the degree of in-plane order, i.e. width of the orientational distribution, can be deciphered from the higher rotational frequencies. We then distinguish this case from a bimodal distribution that represents systems with either some form of AB packing structure (e.g. a herringbone arrangement)[35] or relative conformations of two identical groups within the same molecule (e.g. the terminal methyl groups in the two phospholipid tails). Finally, these theoretical concepts are applied to experimental SFG images of the mixed DPPC : d-POPC monolayers, where we analyze the in-plane orientational distribution of the LC domains, specifically accounting for both the potential angular separation of two acyl tails per lipid molecule and the variation in overall molecular orientations. From this, we gain unprecedented insight into the in-plane distribution of lipid tail-groups and how their long-range packing is expressed heterogeneously across the phase-separated monolayer membrane.

2 Results and discussion

In second-order nonlinear spectroscopy, the measured signals originate from the molecular hyperpolarizability tensor β. The β_{abc} elements express how much polarization is generated in a molecule in coordinate direction a when the system is probed by pulses with polarization b and c.[13–15] As SFG measurements are performed macroscopically and using spatial coordinates in the lab frame (i, j, k), they necessarily yield the macroscopically averaged susceptibility elements $\chi^{(2)}_{ijk}$ rather than individual responses in the molecular frame (a, b, c). These can, however, be readily inter-converted with β_{abc} via an Euler transformation and macroscopic spatial averaging, as shown in eqn (1) (ref. 9, 13 and 36)

$$\chi^{(2)}_{ijk} = \rho \sum_{a=x,y,z} \sum_{b=x,y,z} \sum_{zc=x,y,z} \langle R_{ia} R_{jb} R_{kc} \beta_{abc} \rangle \tag{1}$$

where ρ is the molecular surface density, R_{pq} is the Euler rotation matrix, and $\langle \rangle$ represents orientational averaging over the molecular contributions.

Typically, information on the molecular structure comes from extracting different elements of the susceptibility tensor, which are obtained from SFG

experiments performed under different probe-beam polarization combinations. In order to isolate information on the in-plane structure, a common approach is therefore to use normal incidence illumination and rotate the beam polarization, *i.e.* to switch between probing in the x and y directions.[37,38] However, this cannot provide information on the complete 3D structure of the molecules as no information along z can be obtained. An alternative approach is to simply rotate the sample about the surface normal (*i.e.* azimuthal scanning), thus modulating the in-plane (x, y) contributions whilst leaving the out-of-plane (z) unchanged.[8,9,39] This has the distinct benefit that it still trivially isolates in-plane information but also works with oblique incidence illumination, allowing for simultaneous out-of-plane structural elucidation. Notably, rotating the polarization under oblique illumination also represents a possible approach to achieve similar structural elucidation, however the analysis becomes more complex as the rotation converts between y (S-polarized) and x–z (P-polarized), which would intermix the in-plane and out-of-plane information.

In the azimuthal rotation scheme, the functional form of the nonlinear signal with respect to the sample rotation angle, is determined by the rank of the susceptibility tensor, which is rank-3 in the case of SFG. Each index of the susceptibility tensor represents one of the three spatial axes x, y, and z. Rotating the molecule in the x–y plane by some angle φ then effectively rotates this tensor. Each occurrence of x or y in an element's index introduces a $\cos \varphi$ or $\sin \varphi$ dependence, while an index of z—corresponding to the rotation axis—does not affect its angular dependence. The different elements of $\chi^{(2)}$, which have three indices taking one of the three spatial coordinates, therefore transform as a certain function of $\cos \varphi$ and $\sin \varphi$ with up to cubic dependence. The Fourier transform of the azimuthal rotation angle deconstructs this (up to cubic) function into its Fourier coefficients corresponding to the harmonics of the rotational frequency. Each harmonic will carry information about specific combinations of tensor elements present in the system. For example $\chi^{(2)}_{xxx}$ will have the functional form $\cos^3\varphi$ that is deconstructed into $\frac{1}{4}(3 \cos \varphi + \cos 3\varphi)$ and, as such, will be present in the first and third rotational frequency harmonics, while $\chi^{(2)}_{zzx}$ will have the functional form $\cos \varphi$ and appears in only the first rotational frequency.

The 0-frequency component of the Fourier transform is the rotationally isotropic part of the signal that is unaffected by azimuthal rotation. The $\chi^{(2)}_{zzz}$ element that is fully out-of-plane appears solely in the 0-frequency along with the isotropic components of elements such as $\chi^{(2)}_{xxz}$ that transforms as $\cos^2\varphi = \frac{1}{2}(1 + \cos 2\varphi)$. In-plane signal components that are modulated once over a full azimuthal rotation of the sample appear in the first harmonic, with components that oscillate more frequently being captured by the higher harmonics.

The exact nature of the information contained in the various rotational frequencies and their relationship with each other depends on the symmetry of the molecules under investigation, their spatial distribution, and the polarization combination that is probed in the experiment. The discussion presented in this work offers an intuitive framework as well as mathematical guidelines for extracting structural information from such rotational measurements.

2.1 Simulations

To develop this intuition, we begin with a simple simulation that illustrates how the amplitudes of rotational frequencies depend on the underlying orientational parameters. The orientation of individual molecules on a substrate can be described using the three Euler angles of a specific functional group, as
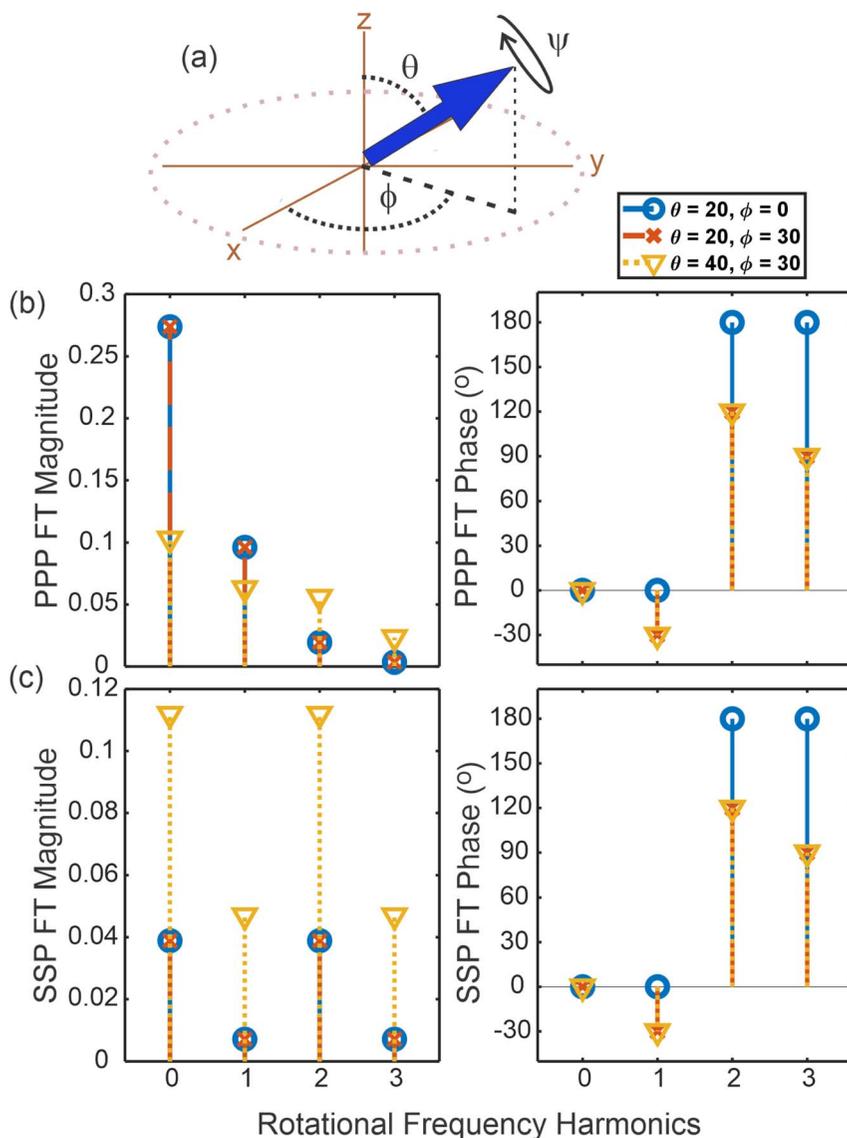

Fig. 2 (a) Molecular orientation with respect to the lab frame z-axis and $x-y$ plane, showing the three Euler angles: θ, ϕ, and ψ. (b) PPP and (c) SSP simulations showing the effect of varying θ and ϕ on the magnitude and phase of the Fourier-transformed rotational frequency harmonics. For the simulations, the probing beam incidence angles are set to 45° (collinear) and the Fresnel factors to 1 for simplicity.

schematically shown in Fig. 2(a), with θ denoting the tilt of the functional group between the z axis and the x–y plane, ϕ the rotation angle within the x–y plane, and ψ the twist angle of the functional group about its own symmetry axis.[9,11,40] In a perfectly ordered "crystalline" sample with only a single orientation in its packing structure, all functional groups would have the same angles θ, ϕ, and ψ. In a less-than-perfectly ordered sample, the molecular distribution would have an average orientation along with a spread in the values of each Euler angle around the ensemble average. The larger the spread, the more disordered the molecules are on the substrate. More complex packing structures would clearly exhibit more complex orientational distribution functions, for example the AB herringbone packing mentioned earlier or molecules with two functional groups per molecule could exhibit bimodal distributions in the three Euler angles.

To demonstrate the impact of molecular geometry and order on the Fourier-transformed rotational SFG signal, we simulate our measurements with a simplified system made up of an ensemble of "molecules" with only a single (normalized) hyperpolarizability element $\beta_{ccc}(=1)$. Under $C_{\infty v}$ symmetry, there are typically three non-zero susceptibility elements for the symmetric stretch: $\beta_{aac} = \beta_{bbc}$, and β_{ccc}.[11] However, the β_{aac} and β_{bbc} elements are governed by the cross-bond polarizability derivative, which is typically small. In our simulations, we are therefore effectively considering the symmetric stretch of a simplistic linear functional group (*e.g.*, C–H or C=O *etc.*) with symmetry $C_{\infty v}$ that only displays a change of polarization along its bond during the vibration. It is, however, important to note that the theoretical considerations discussed in the following are not restricted to this specific case, and can be easily expanded to account for other symmetries.

For the simulations, we set the molecular frame (a, b, c) axes to be initially aligned with the lab frame (x, y, z) coordinates, with the hyperpolarizability tensor then undergoing an Euler transformation to orient the molecule at tilt angle θ, and rotation angle ϕ. Given the choice of the β tensor, the value of the third Euler angle, ψ, is immaterial here (as is true for many symmetries of vibrational modes) and has no effect on the signal.[11]

For an ensemble of 10 000 molecules, the rotation angle of each individual molecule is taken from a wrapped normal distribution with average Φ and spread σ, as in eqn (2).

$$p(\phi, \Phi, \sigma) = \sum_{k=-\infty}^{\infty} \frac{1}{\sqrt{2\pi}\sigma} \exp\left(-\frac{(\phi - \Phi + 2\pi k)^2}{2\sigma^2} \right), \quad 0 \le \phi < 2\pi, \qquad (2)$$

The sample rotation angle φ is then also combined with the angle ϕ of each molecule in the ensemble and, together with θ and ψ, form the Euler rotation matrix R_{ij}. In these simulations, as in the experiments, the sample rotates from 0° to 335° in steps of 45°. The 8 resulting Euler-transformed hyperpolarizability tensors (one for each rotation angle) are Fourier-transformed along the rotation axis, to give four rotational frequencies, denoted as the 0th, 1st, 2nd, and 3rd rotational harmonics (folds).

In general, the magnitude of the signal in each rotational frequency harmonic is determined by the amplitudes of the different hyperpolarizability elements, how they are mapped to the susceptibility tensor in the lab frame, and the

experimental settings such as polarizations, beam geometry (incidence angle(s)), and the Fresnel factors. As discussed above, we are only considering a single hyperpolarizability element for simplicity. With this in mind, for the simulations we also neglect the effects of Fresnel factors (essentially setting them to 1) and apply a collinear beam geometry with an incidence angle of $\theta' = 45°$ such that there are equal x and z contributions from the P-polarized fields.

For the SSP polarization combination, the signals arise from the χ_{yyz} and χ_{yyx} tensor elements, which contribute to the 0th and 2nd folds, and 1st and 3rd folds, respectively, making the magnitude of these pairs of harmonics directly comparable, regardless of any effects from Fresnel factors or the incident angle(s). The amplitude of the Fourier-transformed SFG response as a function of rotational frequency n is given in eqn (3),

$$f_n = (\pm)\frac{1}{2}\sin\theta' \cos\theta \sin^2\theta \, e^{-in\phi} \quad \text{for } n = (0, 2)$$

$$= (\pm)\frac{1}{4}\cos\theta' \sin^3\theta \, e^{-in\phi} \quad \text{for } n = (1, 3)$$

(3)

where the amplitudes are positive for $n = 0, 1$ and negative for $n = 2, 3$. It is worth noting that the factor of -1 in the phase assumes anticlockwise rotation of the sample $x \rightarrow y$ such that φ and ϕ are additive. If clockwise rotation is used, then this phase is simply negated as the Euler and sample rotations become subtractive.

For PPP, things are not quite so simple, even with a collinear beam geometry, as there are four tensor elements contributing: χ_{xxx}, χ_{xxz}, χ_{zzx}, and χ_{zzz}, which have distinct contributions to the different rotational frequencies.[9] This makes the harmonics not as comparable without considering the experimental factors. Under the aforementioned assumptions used in these simulations, the corresponding Fourier-transformed amplitudes are given in eqn (4)–(7).

$$f_0 = \left[-\frac{1}{2}\cos^2\theta' \sin^2\theta + \sin^2\theta' \cos^2\theta\right]\sin\theta' \cos\theta$$

(4)

$$f_1 = \left[-\frac{3}{4}\cos^2\theta' \sin^2\theta + \sin^2\theta' \cos^2\theta\right]\cos\theta' \sin\theta \, e^{-i\phi}$$

(5)

$$f_2 = -\frac{1}{2}\cos^2\theta' \sin\theta' \sin^2\theta \cos\theta \, e^{-2i\phi}$$

(6)

$$f_3 = -\frac{1}{4}\cos^3\theta' \sin^3\theta \, e^{-3i\phi}$$

(7)

Fig. 2(b) and (c) demonstrate the relationship between the Euler angles θ and ϕ and the magnitude and phase of the rotational frequencies in the PPP and SSP polarization combinations, respectively, that are described by eqn (3)–(7). Larger tilt angles θ project the signal more onto the x–y plane. Rotational frequencies that have more in-plane character (χ_{xxx}, χ_{yyx}, etc.) will thus increase more in magnitude with an increase in θ, compared to rotational frequencies that have some out-of-plane character (χ_{zzx}, χ_{yyz}, etc.). This effect is clearly visible in the plots as rotational frequencies that are mainly comprised of out-of-plane signals (such as χ_{zzz} in the 0th harmonic in PPP polarization experiments) sharply

decrease with increasing θ whereas those dominated by in-plane signals (e.g. χ_{xxx} in the PPP 3$^{\text{rd}}$ harmonic) increase. Equally, the 1$^{\text{st}}$ and 3$^{\text{rd}}$ harmonics increase relative to the 0$^{\text{th}}$ and 2$^{\text{nd}}$ in SSP as they arise from χ_{yyx} cf. χ_{yyz}, and thus have a greater in-plane contribution.

On the other hand, as expected, the tilt angle has no effect on the phase of the rotational Fourier transform. The phase of the nonzero rotational frequencies, as seen in eqn (3)–(7), is directly governed by the Euler rotation angle ϕ in the x–y plane. While this may not be immediately obvious from the plots in Fig. 2(b) and (c), this is due to the 2$^{\text{nd}}$ and 3$^{\text{rd}}$ harmonics having negative amplitudes, thus containing an additional phase contribution of 180°. Looking past this, the phases clearly decrease by ϕ for successive harmonics.

In the case of a perfectly crystalline system with the simple packing described above, it is clear that the in-plane angle ϕ can be trivially found from the phase of the rotational frequencies and the tilt angle θ can be extracted from their relative magnitudes. The presence of disorder or more complex packing structures, however, would impact these magnitudes and thus lead to erroneous conclusions regarding the molecular structure and only yield the weighted average direction, Φ.

2.1.1 Effect of disorder. In order to disentangle the statistical spread in the in-plane molecular orientation, the higher rotational frequency harmonics can be used as they are increasingly influenced by any spread in the rotational phase (as shown in eqn (3)–(7) by their $e^{-in\phi}$ dependence). This effect is demonstrated in Fig. 3. For this, we consider two distributions of molecular orientations based on normal distributions with different spreads, namely with $\sigma = 5°$ and $\sigma = 30°$, as shown in Fig. 3(a). Fig. 3(b) then shows the individual contributions to the 1$^{\text{st}}$ (top panel) and 3$^{\text{rd}}$ (middle panel) harmonics, as well as their average (bottom panel). This clearly demonstrates that, with the shorter oscillation period, the higher harmonics are subjected to greater cancellation of the signal when several phase-shifted responses (from molecules at different relative angles) are averaged.

Fig. 3(c) then shows the magnitudes of the Fourier transform harmonics for three distributions: one with no spread, and ones with $\sigma = 30°$ and $\sigma = 60°$. This further emphasizes the stronger effect the distribution width has on the higher harmonics. For example, the broader distribution almost halves the 1$^{\text{st}}$ harmonic yet nearly reduces the 2$^{\text{nd}}$ harmonic to zero.

For some general distribution of molecules, $p(\phi)$ the magnitude of the rotational frequencies in eqn (3)–(7) are now weighted by a cancellation parameter C_n shown in eqn (8). Interestingly, this is nothing other than the Fourier transform of the orientational distribution, as in eqn (9),

$$C_n = \int_0^{2\pi} p(\phi)e^{-in\phi}\mathrm{d}\phi \tag{8}$$

$$= \mathscr{F}\{p(\phi)\} \tag{9}$$

For the normal distribution described by eqn (2), Fig. 3(d) shows the cancellation parameters for each rotational harmonic as a function of the spread, accentuating the effect of orientational disorder on the higher rotational frequencies. Clearly, therefore, the relative magnitudes of the higher harmonics can be used to directly extract the spread in the in-plane distribution. However,
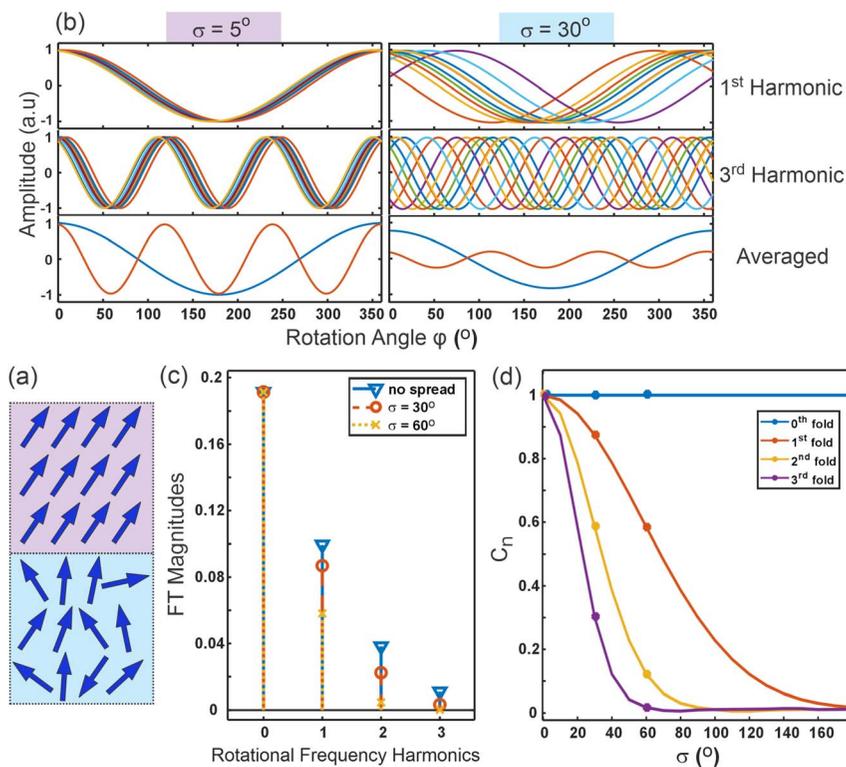
Fig. 3 (a) Schematic of two different in-plane orientational distributions with different spreads, $\sigma = 5°$ (top, purple) and $\sigma = 30°$ (bottom, blue). (b) Plots showing the effect of increasing disorder (spread, σ) on the first (top panel) and third (middle panel) harmonics of a cosine function; the bottom panel shows how much more the averaged signal for the third harmonic is suppressed compared to the first. (c) The simulated effect of increasing disorder from 0° to 30° to 60° on the magnitude of the four rotational frequencies. (d) Plots of the cancellation parameters, C_n for each rotational frequency as a function of the spread in the in-plane distribution.

with such an extra unknown parameter describing the molecular orientation, σ, we now need a minimum of three harmonics to calculate the structural information *i.e.* θ and σ (Note: the additional observable is required to remove the scaling from the hyperpolarizability and molecular density that equally influences all harmonics[9]).

2.1.2 Bimodal distribution of the contributing modes. The model described so far is valid for determining in-plane disorder provided that only a single contribution per molecule is present and the molecules themselves do not adopt a complex packing structure (*e.g.* herringbone). However, as mentioned earlier, many molecules including phospholipids possess two equivalent functional groups, for example the terminal methyl groups on each of the two acyl tails. These equivalent groups contribute to the same vibrational modes but are potentially oriented in different directions, as shown in Fig. 4(a).[41] The in-plane orientation of the molecules obtained from the phase of the rotational Fourier transform in this case is the weighted average orientation of the two branches
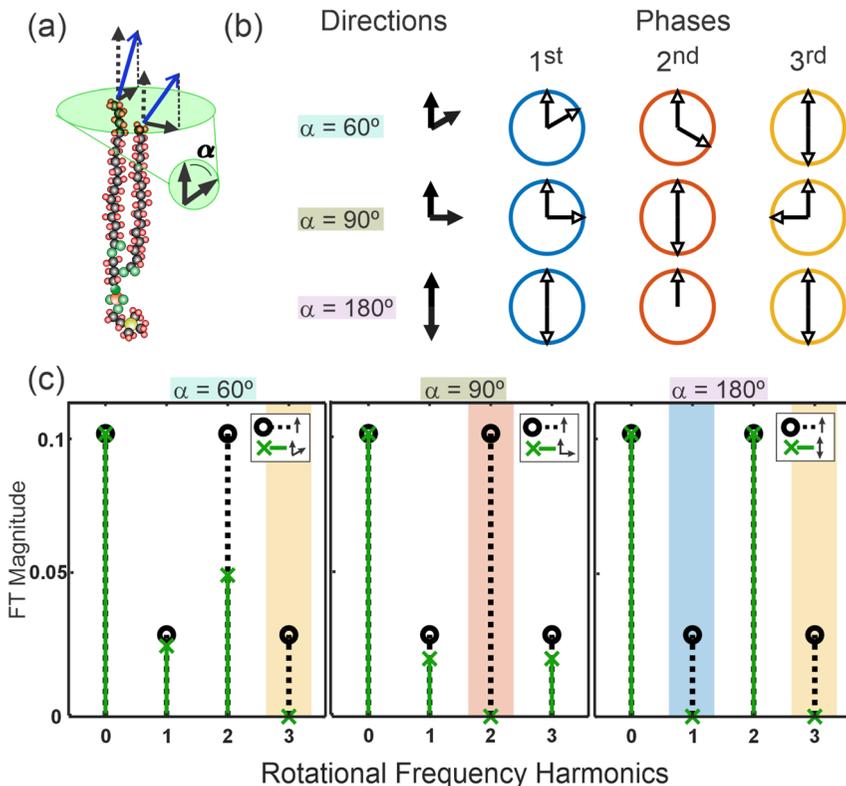
Fig. 4 (a) Structure of DPPC showing the in-plane contribution of the terminal CH_3 symmetric stretch mode from each palmitoyl chain, with an angle α between them. (b) Representation of the rotational phases of the higher harmonics for different separation angles, $\alpha = 60°$, $\alpha = 90°$, and $\alpha = 180°$, showing the separation of the phases is $n \times \alpha$. (c) Comparison of the rotational Fourier transform magnitudes (per CH_3 group) simulated for molecules with only a single palmitoyl chain (black, circles) and molecules with two palmitoyl chains at the separation angles shown in part (b) (green, crosses).

which are fixed at an angle α with respect to each other. Treating this scenario, which exhibits a bimodal distribution, under the above framework of a single gaussian distribution clearly results in an artificially large apparent spread.

Importantly, the fixed angle between the two branches strongly influences the signal strength at higher harmonics. Fig. 4 demonstrates this effect in more detail. Firstly, Fig. 4(b) shows a schematic of the rotational phases of the higher harmonics for selected separation angles of $\alpha = 60°$, $\alpha = 90°$, and $\alpha = 180°$ (here, ignoring any phase contributions from the intrinsic sign of the Fourier response). This essentially shows that the separation of the phases in the nth harmonic are simply $n \times \alpha$. Importantly, this highlights that certain angular separations that correspond to half-integer multiples of the oscillation period of each harmonic lead to complete destructive interference of the signals (opposite phases), *i.e.* 180° in the 1st fold, 90° in the 2nd fold, and both 60° and 180° in the 3rd fold. Equally, separations of an integer multiple of the period create perfect constructive interference, as shown for $\alpha = 180°$ in the 2nd fold. These effects are further

highlighted in Fig. 4(c) which shows the magnitudes of the Fourier transformed harmonics at the same selected separation angles. Overall, this demonstrates that any bimodal nature to the in-plane orientational distribution can lead to strong modulations of the SFG signal rotational frequencies.

To distinguish the angle α between the two moieties and the spread in orientation of the molecules, σ, the orientational distribution becomes a bimodal gaussian, as shown in eqn (10),

$$p(\phi, \Phi, \sigma, \alpha) = \sum_{k=-\infty}^{\infty} \frac{1}{2\sqrt{2\pi}\sigma} \left[\exp\left(-\frac{(\phi - \Phi + \alpha/2 + 2\pi k)^2}{2\sigma^2} \right), \right.$$
$$\left. + \exp\left(-\frac{\phi - \Phi - \alpha/2 + 2\pi k^2}{2\sigma^2} \right) \right], 0 \le \phi < 2\pi \tag{10}$$

An additional free parameter is hence introduced into the cancellation factor $C_n(\sigma, \alpha)$, such that four rotational harmonics are required to determine θ, σ, and α, and remove the scaling of β and ρ on the measured harmonics. Since each rotational SFG measurement should in principle yield rotational frequencies from the 0th to the 3rd fold, such elucidation is theoretically possible from just a single measurement.

2.2 Experimental data

To demonstrate the theoretical concepts described above for determining the in-plane orientational distribution, we now apply these principles to experimental SFG microscopy data from a monolayer of $4:1$ DPPC : d-POPC, probing the CH_3 symmetric stretch of the DPPC tails. As mentioned previously, the first important difference between the calculations shown in the previous section and the experimental data is the form of the hyperpolarizability tensor β. The single nonzero element used in the simulations implies a functional group with $C_{\infty v}$ symmetry and a vanishing cross-bond polarizability derivative. The methyl group, however, falls under the C_{3v} point group, with the symmetric stretch transforming as the A_1 irreducible representation.[11] Ultimately, this yields the same three non-zero elements in the hyperpolarizability tensor as for the symmetric stretch in $C_{\infty v}$: $\beta_{aac} = \beta_{bbc}$, and β_{ccc}. The main distinction is that now the β_{aac} and β_{bbc} components are not solely driven by the cross-bond polarizability derivative of the C–H bonds because of the tetrahedral bond arrangement. In fact, this bond geometry means the hyperpolarizability ratio is $R = \dfrac{\beta_{aac}}{\beta_{ccc}} > 1$.[11,42]

Therefore, considering all three hyperpolarizability components, the expressions for the amplitudes of the 0th and 2nd fold rotational frequency components of $\chi^{(2)}$ now become as in eqn (11)–(14),

$$f_0 = \frac{1}{2} \sin \theta' L_y^{\omega_3} L_y^{\omega_2} L_z^{\omega_1} \rho \beta_{ccc} \cos \theta \left(R + R \cos^2\theta + \sin^2\theta \right) \tag{11}$$

$$f_1 = \frac{1}{4} \cos \theta' L_y^{\omega_3} L_y^{\omega_2} L_x^{\omega_1} \rho \beta_{ccc} \sin \theta \left(3R + R \cos^2\theta + \sin^2\theta \right) e^{-i\phi} \tag{12}$$

$$f_2 = \frac{1}{2} \sin \theta' L_y^{\omega_3} L_y^{\omega_2} L_z^{\omega_1} \rho \beta_{ccc} \cos \theta \left(R - R \cos^2 \theta - \sin^2 \theta \right) e^{-2i\phi} \tag{13}$$

$$f_3 = \frac{1}{4} \cos \theta' L_y^{\omega_3} L_y^{\omega_2} L_x^{\omega_1} \rho \beta_{ccc} \sin \theta \left(R - R \cos^2 \theta - \sin^2 \theta \right) e^{-3i\phi} \tag{14}$$

where all of the factors that influence the amplitudes are now explicitly included, namely the incident beam angle, θ', the Fresnel factors for each frequency ω_q, $L_i^{\omega_q}$, the density, ρ, the different hyperpolarizability components (given here in terms of β_{ccc} and R), and the two relevant Euler angles, θ and ϕ. Clearly, taking $R = 0$ yields the same expressions as in eqn (3), as expected. Importantly, however, this also shows that nonzero values of R highly influence the magnitudes of the different rotational frequencies.

This sensitivity of the different rotational harmonics to R is highlighted in Fig. 5(c), which plots the ratios of 0th to 2nd and 1st to 3rd harmonic magnitudes. Although in the $C_{\infty v}$ symmetry group R is nothing other than the ratio of the cross-bond to along-bond polarizability derivatives and is therefore typically small (e.g. $R \approx 0.08$ for the C=O group[43]), this plot shows that even small values of R can lead to non-negligible deviations to the amplitudes of the observed rotational harmonics. In this context, it is therefore worth noting that, despite assuming constant cross-bond polarizability during the vibration (i.e. $R = 0$), the theoretical concepts discussed above still hold for non-negligible values of R, as well as for other symmetry groups. This assumption served only to simplify the expressions for the sake of clarity in demonstrating the concepts in structural elucidation. Nevertheless, this clearly shows that a detailed analysis of the rotational harmonics generally requires an accurate value for R.

Using the expressions in eqn (11)–(14) and multiplying them by the bimodal distribution from eqn (10), the experimental magnitudes are subject to six free parameters: ρ, β_{ccc}, R, θ, σ, and α. Given that the signal amplitudes are all equally scaled by both ρ and β_{ccc}, they can essentially be treated as a single unknown parameter i.e. $\rho \times \beta_{ccc}$. This nevertheless shows that a minimum of five observables are required for determining the structure, necessitating using more than one polarization combination.
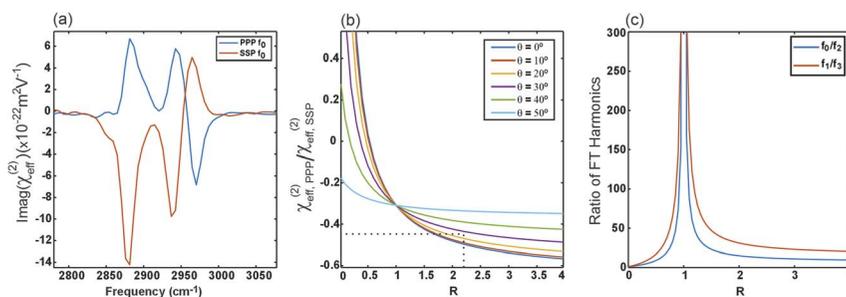

Fig. 5 (a) DPPC LC phase 0th rotational frequency spectra from PPP and SSP experiments, still including the Fresnel factors and the influence of the incidence angle. (b) Simulated values of the ratio of PPP to SSP 0th rotational frequency amplitudes as a function of hyperpolarizability ratio R at different values of tilt angle θ. (c) Dependence of the magnitude ratios of the SSP Fourier-transformed rotational harmonics on R, assuming $C_n(\sigma, \alpha) = 1$ and taking $\theta = 27°$.

From a practical standpoint, when probing the CH_3 symmetric stretch, the higher harmonics are intrinsically suppressed by the large value of R, and are also more susceptible to signal cancellation from the two tails and any orientational disorder. They therefore yield significantly reduced signal-to-noise ratios. To simplify the analysis and obtain the best possible confidence in any structural conclusions, we thus exploit the well-established literature value for $R = 2.2$,[9,11] as well as amplitudes from both the SSP and PPP polarization combinations.

2.2.1 Determining the tilt angle. Using the ratio of $\chi_{PPP}^{(2)}$ and $\chi_{SSP}^{(2)}$ amplitudes is a common approach for deducing the tilt angle in SFG spectroscopy, albeit under the assumption of in-plane isotropy.[12] This is equivalent to taking the 0th fold components of the rotational Fourier transform in a system displaying in-plane anisotropy. By combining the above expression for f_0 in SSP from eqn (11)–(14) with that for PPP given in eqn (15),

$$
\chi_{PPP,f_0}^{(2)} = \left[-\frac{1}{2}\cos^2\theta' L_x^{\omega_2} L_x^{\omega_3} \left(R + R\cos^2\theta + \sin^2\theta\right) \right.
$$
$$
\left. + \sin^2\theta' L_z^{\omega_2} L_z^{\omega_3} \left(R\sin^2\theta + \cos^2\theta\right) \right] \tag{15}
$$
$$
\times \sin\theta' L_z^{\omega_1} \rho\beta_{ccc} \cos\theta
$$

it is clear that their ratio is only a function of R and θ. Therefore, using the literature value of $R = 2.2$, as mentioned above, the ratio of the amplitudes for the symmetric methyl stretch can yield θ independent of the other structural parameters. It is, however, worth noting that this is sensitive to the exact value of R, as shown in Fig. 5(b). Equally, while we discussed above that the ratios between the harmonics are also sensitive to any deviations in R, within the expected range for the methyl symmetric stretch (around 2.2), the slopes in Fig. 5(c) are comparatively flat.

Fig. 5(a) shows the 0-fold spectra from the SSP and PPP polarization experiments, averaged over all pixels containing LC domains, where the CH_3 symmetric stretch gives rise to the resonance at 2881 cm^{-1}.[12] Taking the amplitudes at this frequency then yields a ratio of -0.47, ultimately corresponding to a tilt angle of $\theta = 27°$, which, given the tetrahedral bond geometry in the acyl tails, corresponds to the tail-groups being almost completely upright, as expected.

2.2.2 Determining the in-plane distribution. Having established the methyl tilt angle, the magnitudes from the higher harmonics can then be used to gain insight into the in-plane distribution, deducing values for the spread and in-plane separation angle. Using all three harmonics thus implies an over-determined problem that can yield better confidence in the obtained structural information.

To achieve this, the cancellation factors $C_n(\sigma, \alpha)$ for each of the higher harmonics are calculated from their spectral magnitudes. This is done by comparing the experimental magnitudes to those expected for a system with no cancellation, calculated using the values of R and θ. Again, in order to remove the amplitude scaling from $\rho\beta_{ccc}$, the magnitudes of the higher harmonics are divided by the 0th fold magnitude. This procedure can be expressed mathematically by considering the magnitude of the nth harmonic, A_n, as in eqn (16),

$$
A_n = |f_n(R,\theta,\rho\beta_{ccc})| C_n(\sigma,\alpha) \tag{16}
$$

which is expressed as the product of the cancellation parameter and the harmonic frequency function, f_n (e.g., like those given in eqn (11)–(14)), which essentially describes the intrinsic ratios of the different harmonics for a perfectly ordered distribution described by a δ-function. The cancellation parameter is thus given as in eqn (17),

$$C_n(\sigma, \alpha) = \frac{f_n(R, \theta, \rho\beta_{\mathrm{ccc}})C_n}{f_n(R, \theta, \rho\beta_{\mathrm{ccc}})} = \frac{\dfrac{A_n, \exp}{A_0, \exp}}{\dfrac{A_n, \mathrm{sim}}{A_0, \mathrm{sim}}} \tag{17}$$

where $A_{n,\exp}$ is the experimental magnitude of the nth harmonic, and $A_{n,\mathrm{sim}}$ is the magnitude of the nth harmonic calculated from R and θ, assuming $C_n(\sigma, \alpha) = 1$.

Having extracted the cancellation parameters, they can be compared to simulated values for a given combination of α and σ. Fig. 6(a) presents these simulated cancellation parameters for the 1st, 2nd, and 3rd harmonics as 2D plots for $0 \leq \alpha \leq 180°$ and $0 < \sigma \leq 90°$. These show the expected behavior for the different rotational frequencies, clearly highlighting the zero-lines for $\alpha = \dfrac{(2k+1) \times 180°}{n}$ (for integer k), as well as the gradual decrease for larger σ, with this effect becoming increasingly prominent in the higher harmonics.

Fig. 6(b) then shows the magnitude spectra for each harmonic at the methyl symmetric stretch frequency used in this calculation. This emphasizes the aforementioned point that the higher harmonics yield significantly reduced
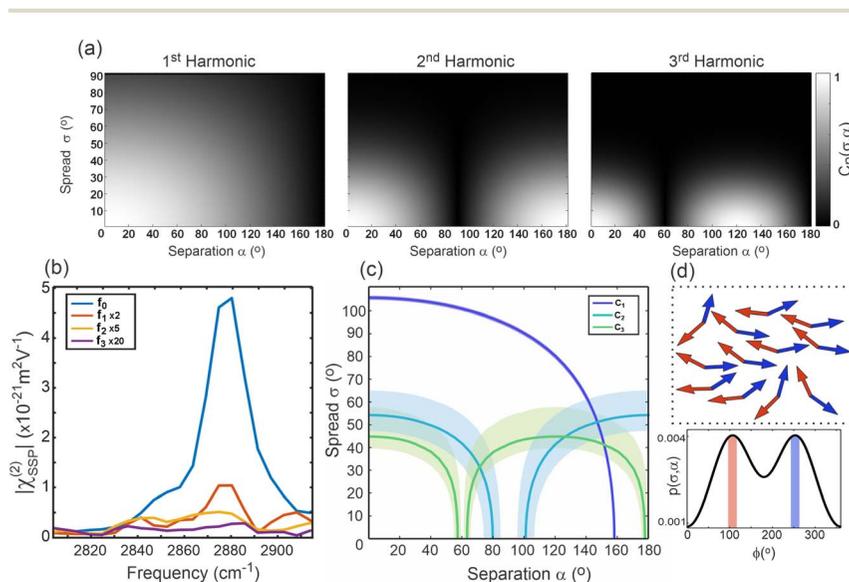

Fig. 6 (a) 2D Plots showing the calculated cancellation parameters, C_n, for the 1st, 2nd, and 3rd harmonics as a function of the spread, σ, and separation angle of the two methyl groups, α. (b) Magnitudes of the SSP rotational harmonics, having removed the Fresnel factors and the scaling due to the incidence angle. (c) Contour values based on the calculated cancellation factors C_n. Uncertainties are estimated from the standard deviation in the spectral noise shown in part (b). (d) Schematic of the predicted orientational spread and separation angle between palmitoyl chains.

signal-to-noise spectra, in part due to their inherent suppression due to the value of R, as well as due to their sensitivity to the orientational distribution. Nevertheless, the spectra clearly show a pronounced peak at the expected frequency of approximately 2881 cm^{-1} in the 0th and 1st fold contributions, with the 2nd and 3rd fold harmonics yielding slight indications of an increased magnitude at these frequencies compared to the noise floor.

By extracting the spectral magnitudes from Fig. 6(b), the set of cancellation parameters for the higher harmonics can be calculated (importantly also accounting for contributions from the noise floor). Contour plots at the values for these cancellation parameters can then be drawn in the α–σ parameter space. These are shown in Fig. 6(c), also including uncertainty ranges estimated from the standard deviation of the spectral noise. This analysis clearly only yields a single confined region in the α–σ parameter space that satisfies all three cancellation parameters. This region corresponds to an in-plane orientational spread of around 45–55° for the DPPC molecules, with an in-plane separation angle of the two palmitoyl chains of approximately 150°. A schematic of this structure and the in-plane orientational distribution is shown in Fig. 6(d).

These extracted values for the in-plane orientational distribution indicate that, within the resolution of the microscope (approx. 1 μm (ref. 44)), the LC domains exhibit a relatively large amount of in-plane orientational disorder, with 68% of molecules being directed within a cone of ~100°. That being said, 1 μm^2 corresponds to approximately 2 million molecules,[10] and the liquid crystalline nature of the phase structure suggests a significant degree of orientational freedom. Equally, as the lateral interactions are dominated by weak van der Waals forces between the tail-groups,[39,45–47] it is expected that entropy still plays a significant role in the packing structure. On the other hand, confining millions of molecules to an in-plane cone angle of ~100° clearly does fit with the degree of short-range order that would be expected in order to result in the long-range ordered packing that we observe at the microscale. Nevertheless, the precise nature of the short-range packing and exactly how it is translated into the long-range order remains an open question.

The finding of the in-plane separation of the two lipid tail-groups to be ~150° is also interesting, as it clearly shows that the adopted packing structure is generated by a molecular conformation with vastly different orientations of its two acyl chains. This implies that this specific molecular conformation is conducive to optimizing the intermolecular interactions. It would thus be interesting to investigate this further to build up a more complete picture of the molecular conformation within the LC domain packing structure.

It is worth noting that the values extracted using the theoretical concepts presented in this work are based on important structural assumptions. Firstly, they are only valid if the in-plane distribution can be well-represented by a bimodal gaussian function. Equally, we have assumed that the out-of-plane tilt angles for the two tail methyl groups are both equal and present a narrow distribution, *i.e.* the distribution of θ can be represented by a δ-function. While this assumption may seem contradictory to the finding of substantially different in-plane orientations of the two tails, the tilt angle is governed by the out-of-plane anisotropy in the system, and thus is determined by the strongly amphiphilic nature of the lipids that drives their self-assembly. This driving force to generate

largely upright tails is therefore expected to create a sufficiently narrow distribution for θ such that this assumption is reasonable.

Finally, as noted earlier, the extracted values are dependent on the literature value of R being valid. Nevertheless, in the above discussion we showed that R can, in theory, also be treated as a free parameter and be determined using the experimental amplitudes. Equally, the presented concepts can also be trivially expanded to account for more complex orientational distributions, allowing for more defining parameters and degrees of freedom. Increasing the number of parameters to be determined, including R, however, necessarily requires both high precision SFG measurements and more observables, *e.g.* the use of more polarization combinations or the inclusion of other vibrational modes such as the CH_3 antisymmetric stretches.

3 Conclusions

The presence of long-range orientational order in thin molecular films hinges on strong short-range orientational correlations between neighboring molecules. Understanding the origins from which this mesoscopic anisotropy emerges requires a detailed picture of these correlations on the molecular scale, as well as their correspondence to molecular geometry and packing conformation.

Vibrational sum-frequency generation microscopy is uniquely capable of providing insight not only on the chemical composition and packing geometry but also on how ordered the arrangement of molecules is within the film. By azimuthally rotating the sample and applying a Fourier transform with respect to the rotation angle, both the in-plane and out-of-plane molecular orientations can be elucidated through the analysis of the phase and magnitude of the 0th and 1st harmonic rotational frequencies. Given the sensitivity of the SFG signal strength to local asymmetry, decreased anisotropy due to disorder in the arrangement of molecules leads to cancellation of the SFG signal and thus decreased magnitudes. Higher rotational frequencies are more susceptible to such cancellation and are therefore exploited here to extract the degree of disorder in the system.

The magnitudes of the rotational frequencies depend on the value of the out-of-plane tilt angle of the molecules, the ratios of different hyperpolarizability components, R, and the molecular density in the films. Furthermore, the higher harmonics are also modulated by a cancellation factor that is a function of the statistical distribution of the vibrational mode being probed. In the case of a monolayer of 4 : 1 DPPC : d-POPC, the terminal methyl symmetric stretch is used to report on the relative orientation of the two hydrophobic acyl chains in DPPC molecules in phase-separated semi-ordered condensed regions. As each molecule contains two of such methyl groups (one per acyl tail), the in-plane orientation of these modes is modelled as a bimodal distribution with a fixed angle separating the two methyl groups, and a spread corresponding to the variations of molecular directions.

The average tilt angle of the methyl groups was determined from the ratio of 0th harmonic frequency amplitudes of experiments done in SSP and PPP polarization combinations, together with the accepted literature value of 2.2 for R in methyl groups.[11] The tilt angle was found to be 27°, which fits with the expected structure of the acyl tails pointing almost upright at the surface. The cancellation factors in SFG rotational magnitudes were estimated through an analysis of the

higher SSP rotational harmonics, suggesting they have a distribution with spread $\sigma \approx 50°$ and a fixed in-plane separation angle $\alpha \approx 150°$ between the methyl groups on the two acyl chains.

To further corroborate the inferred conformations and orientational distribution of DPPC molecules in thin films, additional experiments are required, including selective deuteration of different moieties across the two acyl chains as well as measurements targeting other functional groups within the lipid.[48–50]

It is important to note that these calculations rely on accurate values of the hyperpolarizability ratio, R. Uncertainty in R can introduce errors in the extracted tilt angle, which then propagate into the other structural parameters. In principle, improved precision and signal-to-noise ratios in the measured amplitudes of higher rotational harmonics would enable direct determination of R for these functional groups from the SFG measurements themselves. To that end, one potential avenue for improvement lies in increasing the accuracy of the measured spectral amplitude and phase during the rotational measurements by systematically tracking and correcting errors using simultaneous referencing, an approach that is the focus of current work.

Overall, the presented theoretical concepts surrounding the analysis of the different Fourier-transformed rotational frequency harmonics in SFG microscopy measurements with azimuthal scanning, clearly offer enhanced structural investigations into anisotropic and heterogeneous systems. The showcased example application to phase-separated lipid monolayers yielded far greater insight into the specific molecular conformation and in-plane orientational distribution within the microscopically ordered domains than has been previously possible, highlighting the potential of this method for further studies into the structure of model membranes. Beyond this, SFG microscopy is broadly applicable and thus such structural elucidation is expected to offer greater characterization capabilities across a wide range of samples, spanning molecular films to inorganic materials.[51–61]

4 Experimental methods

4.1 Sample preparation

Detailed sample preparation can be found in the literature.[8] The lipids 1,2-dipalmitoyl-*sn*-glycero-3-phosphocholine (DPPC, >99%), and d_{82}-1-palmitoyl-2-oleoyl-*glycero*-3-phosphocholine (d-POPC, >99%) were purchased from Avanti Polar Lipids (Alabaster, AL, USA). The lipids were dissolved in chloroform (99.0–99.4% purity, VWR International GmbH, Darmstadt, Germany) to make stock solutions at a concentration of 1 mg mL^{-1}. Phase separated lipid samples were made by mixing DPPC and d-POPC lipids in mass ratios of 4 : 1, respectively, and depositing them dropwise onto the water surface of a PTFE Langmuir–Blodgett trough (MicroTrough G1, Kibron, Helsinki, Finland) filled with ultrapure water (Milli-Q, 18.2, MΩ, cm, <3 ppb total organic carbon) with surface pressure variation within 0.1 mN m^{-1} under full compression. After deposition, the films were left undisturbed for approximately 5 minutes to allow for the evaporation of chloroform. The monolayers were then compressed to a surface pressure of 20 mN m^{-1} at a barrier speed of 10 mm min^{-1} and equilibrated for 2 hours to ensure stabilization and oxidation of the dPOPC lipid by ambient ozone exposure.[62]

The Langmuir–Blodgett transfer method was employed to suppress both intrinsic dynamic motion and convection-driven flows[63,64] by immobilizing the monolayers for microscopy measurements onto ultra-flat fused silica substrates (Korth Kristalle, Altenholz, Germany, 5 mm thickness, 25.4 mm diameter, <2 nm surface roughness). Monolayers were transferred at a rate of 2 mm min^{-1} using a LayerX dipper (Kibron, Helsinki, Finland). The substrates were cleaned with chloroform and ultrapure water, followed by UV-ozone treatment (UV/Ozone ProCleaner Plus, BioForce Nanosciences, Virginia Beach, VA, USA) for at least 30 minutes prior to use.

4.2 SFG microscope

A full dataset is a 4-dimensional set of hyperspectral images at different rotational frequencies. Data along the spectral frequency dimension is obtained from the time-domain measurement of the SFG signal in a home-built interferometer by scanning the delay between an IR pulse centered at 2900 cm^{-1} (light conversion TOPAS pumped by Coherent Astrella Ti : sapphire system) and a visible up-converter pulse at 690 nm, generated by doubling the output of a second TOPAS. These scans span −300 to 3000 fs with steps of 2 fs and are Fourier-transformed to obtain hyperspectral images. The phase of the spectra is obtained by heterodyning the sample SFG signal with a local oscillator (LO) generated by SFG on a z-cut quartz crystal in a collinear geometry. The spectra are then normalized in phase and amplitude using a reference measurement of z-cut quartz (from −300 to 300 fs). Measurements are averaged over 8 interferometric scans and a linear nonresonant baseline is subtracted from the spectra in post-processing.

Wide-field images are obtained by focusing the IR, visible and LO beams on the sample at an incidence angle of 36° using a 38 cm focal length off-axis parabolic mirror and a custom-built reflective objective (0.78 NA, Pike Technologies, Madison, WI, USA), and detecting the spectrally filtered SFG signal on a cooled CCD camera (ProEM-HS: 1024BX3, Teledyne Princeton Instruments, Trenton, NJ, USA). Details about the design and integration of the home-built interferometer into the microscope as well as noise removal using paired pixel balanced detection can be found in previous publications.[44,65]

Data along the fourth (rotational) dimension were acquired by rotating the sample azimuthally in increments of 45° and acquiring SFG spectral images at each angle. Corresponding pixels at each angle were aligned together by back rotating the images and using a Fourier transform cross-correlation algorithm to shift the pixels on top of each other. The data was then Fourier transformed along the azimuthal rotation angle axis to obtain rotational frequencies. Average spectra $(\mathrm{Im}(\chi^{(2)}))$ at each rotational frequency were obtained by subtracting the rotational phase of the 1$^{\mathrm{st}}$ fold from the phase of all higher harmonics at the CH$_3$ symmetric stretch frequency, to be able to use the real part of the rotational Fourier transform in calculating the average.

Author contributions

NM – methodology, formal analysis, investigation, visualization, writing – original draft. BJ – investigation, formal analysis, writing – review & editing. MW –

resources, writing – review & editing, supervision, funding acquisition. MT – conceptualization, methodology, writing – review & editing. APF – conceptualization, methodology, formal analysis, investigation, writing – review & editing, supervision.

Conflicts of interest

There are no conflicts to declare.

Data availability

Data for this article are available in the Zenodo repository at the following DOI: https://www.doi.org/10.5281/zenodo.18223015.

Acknowledgements

Notes and references

1 L. A. Pettersson, S. Ghosh and O. Inganäs, *Org. Electron.*, 2002, **3**, 143–148.
2 D. J. Ellison, B. Lee, V. Podzorov and C. D. Frisbie, *Adv. Mater.*, 2011, **23**, 502–507.
3 N. Crivillers, A. Liscio, F. D. Stasio, C. V. Dyck, S. Osella, D. Cornil, S. Mian, G. M. Lazzerini, O. Fenwick, E. Orgiu, F. Reinders, S. Braun, M. Fahlman, M. Mayor, J. Cornil, V. Palermo, F. Cacialli and P. Samorì, *Phys. Chem. Chem. Phys.*, 2011, **13**, 14302–14310.
4 T. Surrey and F. Jähnig, *Proc. Natl. Acad. Sci. U. S. A.*, 1992, **89**, 7457–7461.
5 J. H. Lorent, K. R. Levental, L. Ganesan, G. Rivera-Longsworth, E. Sezgin, M. Doktorova, E. Lyman and I. Levental, *Nat. Chem. Biol.*, 2020, **16**, 644–652.
6 I. Levental, K. R. Levental and F. A. Heberle, *Trends Cell Biol.*, 2020, **30**, 341–353.
7 K. Simons and E. Ikonen, *Nature*, 1997, **387**, 569–572.
8 A. P. Fellows, B. John, M. Wolf and M. Thämer, *Nat. Commun.*, 2024, **15**, 3161.
9 A. P. Fellows, B. John, M. Wolf and M. Thaämer, *J. Phys. Chem. Lett.*, 2024, **15**, 10849–10857.
10 B. John, S. Kaur, M. Wolf, M. Thämer and A. P. Fellows, *Faraday Discuss.*, 2025, **259**, 366–383.
11 H.-F. Wang, W. Gan, R. Lu, Y. Rao and B.-H. Wu, *Int. Rev. Phys. Chem.*, 2005, **24**, 191–256.
12 A. G. Lambert, P. B. Davies and D. J. Neivandt, *Appl. Spectrosc. Rev.*, 2005, **40**, 103–145.
13 Y. Shen, *Annu. Rev. Phys. Chem.*, 2013, **64**, 129–150.
14 R. W. Boyd, *Nonlinear Optics*, Elsevier, 2008.
15 A. Morita, *Theory of Sum Frequency Generation Spectroscopy*, Springer Nature Singapore, 2018.
16 R. Superfine, J. Y. Huang and Y. R. Shen, *Chem. Phys. Lett.*, 1990, **172**, 303–306.
17 R. Superfine, J. Y. Huang and Y. R. Shen, *Opt. Lett.*, 1990, **15**, 1276–1278.
18 S. Yamaguchi and T. Otosu, *Phys. Chem. Chem. Phys.*, 2021, **23**, 18253–18267.

19 H. Wang and W. Xiong, *Annu. Rev. Phys. Chem.*, 2021, **72**, 1–28.

20 L. Fu, Z. Wang, V. S. Batista and E. C. Y. Yan, *J. Diabetes Res.*, 2016, **2016**, 7293063.

21 S. Hosseinpour, S. J. Roeters, M. Bonn, W. Peukert, S. Woutersen and T. Weidner, *Chem. Rev.*, 2020, **120**, 3420–3465.

22 S. A. Shah and S. Baldelli, *Acc. Chem. Res.*, 2020, **53**, 1139–1150.

23 S. A. Hall, K. C. Jena, P. A. Covert, S. Roy, T. G. Trudeau and D. K. Hore, *J. Phys. Chem. B*, 2014, **118**, 5617–5636.

24 J. Dedic, H. Okur and S. Roke, *Frontiers in Optics/Laser Science*, 2018, FM4B.3.

25 S. Roke, *ChemPhysChem*, 2009, **10**, 1380–1388.

26 X. Chen, M. L. Clarke, J. Wang and Z. Chen, *Int. J. Mod. Phys. B*, 2005, **19**, 691–713.

27 K.-K. Hung, U. Stege and D. K. Hore, *Appl. Spectrosc. Rev.*, 2015, **50**, 351–376.

28 E. C. Y. Yan, L. Fu, Z. Wang and W. Liu, *Chem. Rev.*, 2014, **114**, 8471–8498.

29 F. Yesudas, M. Mero, J. Kneipp and Z. Heiner, *J. Chem. Phys.*, 2018, **148**, 104702.

30 K. A. Cimatu and S. Baldelli, *J. Phys. Chem. C*, 2009, **113**, 16575–16588.

31 S. M. Ortiz and S. Baldelli, *Surf. Sci.*, 2025, **751**, 122627.

32 K. Kuhnke, D. M. P. Hoffmann, X. C. Wu, A. M. Bittner and K. Kern, *Appl. Phys. Lett.*, 2003, **83**, 3830–3832.

33 C.-Y. C. J. Boik and E. O. Potma, *Annu. Rev. Phys. Chem.*, 2013, **64**, 77–99.

34 A. Sakurai, S. Takahashi, T. Mochizuki and T. Sugimoto, *Nano Lett.*, 2025, **25**, 6390–6398.

35 P. M. Claesson, N. A. Wojas, R. Corkery, A. Dedinaite, J. Schoelkopf and E. Tyrode, *Phys. Chem. Chem. Phys.*, 2024, **26**, 2780–2805.

36 H.-F. Wang, L. Velarde, W. Gan and L. Fu, *Annu. Rev. Phys. Chem.*, 2015, **66**, 1–28.

37 K. Y. Raygoza-Sánchez, I. Rocha-Mendoza, P. Segovia, A. V. Krasavin, G. Marino, T. Cesca, N. Michieli, G. Mattei, A. V. Zayats and R. Rangel-Rojo, *Sci. Rep.*, 2019, **9**, 11514.

38 C. Teulon, I. Gusachenko, G. Latour and M.-C. Schanne-Klein, *Opt. Express*, 2015, **23**, 9313–9328.

39 N. A. Wojas, E. Tyrode, R. Corkery, M. Ernstsson, V. Wallqvist, M. Järn, A. Swerin, J. Schoelkopf, P. A. C. Gane and P. M. Claesson, *Langmuir*, 2023, **39**, 14840–14852.

40 G. J. Simpson, *Nonlinear Optical Polarization Analysis in Chemistry and Biology*, Cambridge University Press, 2017.

41 A. P. Fellows, M. T. L. Casford and P. B. Davies, *AIP Adv.*, 2021, **11**, 045119.

42 X. Zhuang, P. B. Miranda, D. Kim and Y. R. Shen, *Phys. Rev. B:Condens. Matter Mater. Phys.*, 1998, **59**, 12632–12640.

43 X. Li, V. Pramhaas, C. Rameshan, P. Blaha and G. Rupprechter, *J. Phys. Chem. C*, 2020, **124**, 18102–18111.

44 T. Khan, B. John, R. Niemann, A. Paarmann, M. Wolf and M. Thämer, *Opt. Express*, 2023, **31**, 28792.

45 C. L. Wennberg, D. v. d. Spoel and J. S. Hub, *J. Am. Chem. Soc.*, 2012, **134**, 5351–5361.

46 A. J. Kox, J. P. J. Michels and F. W. Wiegel, *Nature*, 1980, **287**, 317–319.

47 J. N. Israelachvili, *Intermolecular and Surface Forces*, Elsevier, 2011.

48 G. Ma and H. C. Allen, *Langmuir*, 2006, **22**, 5341–5349.

49 E. Navakauskas, G. Niaura and S. Strazdaite, *Colloids Surf., B*, 2022, **220**, 112866.

50 A. P. Fellows, M. T. Casford and P. B. Davies, *Biophys. J.*, 2023, **122**, 2007–2022.

51 N. S. Mueller, A. P. Fellows, B. John, A. E. Naclerio, C. Carbogno, K. Gharagozloo-Hubmann, D. Baláž, R. A. Kowalski, H. H. Heenen, C. Scheurer, K. Reuter, J. D. Caldwell, M. Wolf, P. R. Kidambi, M. Thämer and A. Paarmann, *Adv. Mater.*, 2025, e10124.

52 Y. Behovits, A. L. Chekhov, A. Ruge, R. Rouzegar, B. R. Serrano, A. P. Fellows, B. John, M. Thämer, S. Reimers, F. Renner, T. Dannegger, U. Nowak, T. S. Seifert, M. Kläui, M. Jourdan and T. Kampfrath, *arXiv*, 2025, preprint, arXiv:2512.23397, DOI: 10.48550/arXiv.2512.23397.

53 A. Hanninen, M. W. Shu and E. O. Potma, *Biomed. Opt. Express*, 2017, **8**, 4230.

54 H. Wang, T. Gao and W. Xiong, *ACS Photonics*, 2017, **4**, 1839–1845.

55 V. Raghunathan, Y. Han, O. Korth, N.-H. Ge and E. O. Potma, *Opt. Lett.*, 2011, **36**, 3891.

56 J. C. Wagner, Z. Wu, H. Wang and W. Xiong, *J. Phys. Chem. B*, 2022, **126**, 7192–7201.

57 H. Wang, W. Chen, J. C. Wagner and W. Xiong, *J. Phys. Chem. B*, 2019, **123**, 6212–6221.

58 J. H. Jang, J. Jacob, G. Santos, T. R. Lee and S. Baldelli, *J. Phys. Chem. C*, 2013, **117**, 15192–15202.

59 Y. Han, J. Hsu, N.-H. Ge and E. O. Potma, *J. Phys. Chem. B*, 2015, **119**, 3356–3365.

60 K. Inoue, M. Fujii and M. Sakai, *Appl. Spectrosc.*, 2009, **64**, 275–281.

61 H. Maekawa, S. K. K. Kumar, S. S. Mukherjee and N.-H. Ge, *J. Phys. Chem. B*, 2021, **125**, 9507–9516.

62 L. Qiao, A. Ge, Y. Liang and S. Ye, *J. Phys. Chem. B*, 2015, **119**, 14188–14199.

63 E. H. G. Backus, D. Bonn, S. Cantin, S. Roke and M. Bonn, *J. Phys. Chem. B*, 2012, **116**, 2703–2712.

64 A. P. Fellows, M. T. L. Casford and P. B. Davies, *J. Chem. Phys.*, 2022, **156**, 164701.

65 M. Thämer, R. K. Campen and M. Wolf, *Phys. Chem. Chem. Phys.*, 2018, **20**, 25875–25882.